A Deep Learning Framework for Multi-Source EEG Localization

C. Buda, B. Gambosi (IEEE EMBS Member), N. Toschi* (IEEE Senior Member),
and L. Astolfi* (IEEE EMBS Member)

***Abstract*— Electroencephalography (EEG) provides millisecond-scale resolution of neural activity but struggles to accurately localize multiple concurrent sources, especially in spatially close regions. Classical linear inverse methods, such as MNE, sLORETA, and dSPM, address the ill-posed inverse problem through regularization but often exhibit a "single-source bias", suppressing smaller generators. This paper introduces a deep learning framework designed to robustly identify multiple sources of activity from short EEG segments. Our approach leverages a realistic simulation pipeline that systematically generates EEG recordings from physiologically plausible, distributed current sources. We train a convolutional neural network (ConvNET) on thousands of such simulations, ensuring generalization by using a forward model distinct from that of classical solvers, thereby minimizing the risk of an "inverse crime". We evaluate our ConvNet against nine well-established inverse solvers (MNE, dSPM, sLORETA, eLORETA, LORETA, LAURA, and depth-weighted variants). Benchmarking across multiple synthetic test scenarios demonstrates that our method consistently outperforms traditional solvers, particularly in resolving closely spaced sources, while maintaining or improving accuracy for single-source cases. These results highlight the potential of deep learning to overcome biases in EEG source imaging, offering a more reliable approach for multi-source localization.**

***Clinical relevance*— By leveraging deep learning, our approach improves localization accuracy, particularly in closely spaced or deep brain sources, potentially enhancing presurgical planning, brain-computer interfaces, and real-time neurofeedback applications.**

I. INTRODUCTION

Neuroimaging techniques have been dominated by magnetic resonance imaging (MRI) over the last three decades, enabling an extraordinary level of spatial resolution when mapping functional brain activity [1]. Despite its strong advantages, MRI is expensive and often less convenient for capturing rapid neural dynamics. In contrast, electroencephalography (EEG) has the notable strength of capturing brain electrophysiological activity at millisecond time scales, making it an excellent tool for tracking fast neural events. Unfortunately, the extraction of accurate, high-resolution source localizations from EEG remains difficult.

A principal challenge stems from the ill-posed nature of the inverse problem: many different current distributions in the brain can produce essentially the same scalp potential at the (finite number of) electrodes. Traditional linear inverse approaches (for instance, minimum-norm estimates (MNE) [2], sLORETA [3], dSPM [5], or LAURA [4]) impose regularizing assumptions to constrain solutions. While these methods are computationally efficient and grounded in well-established mathematical theory, they often struggle to detect more than one source of activity.

Recent studies leveraging deep learning have shown promise in EEG source imaging. Neural networks can learn complex, non-linear mappings from scalp potentials to underlying neural activity without relying on strong spatial priors [6], [7]. While these advances highlight the potential of data-driven solutions, applications to multi-source localization —where multiple, spatially distributed neural generators must be identified simultaneously— remain under-explored.

In this work, we introduce a deep learning approach for multi-source EEG localization. We design a simulation pipeline capable of generating realistic, distributed current sources with physiologically plausible correlations and variable spatial extents. By training our model on thousands of such diverse patterns, we enable it to disentangle overlapping source activity, improving robustness to complex configurations. Crucially, we expose the network to a broad range of cortical regions, ensuring generalizability across different activation patterns. To mitigate the risk of an inverse crime, we employ separate head models and forward operators —one for generating simulated scalp potentials and another, slightly perturbed model for benchmarking classical solvers— preventing trivial advantages from exact forward model matching.

We evaluate the trained convolutional neural network (ConvNet) on test cases designed to assess localization accuracy for multiple, simultaneously active sources. We compare performance against nine classical solvers implemented with well-known toolboxes, including variants of MNE, dSPM, sLORETA, eLORETA, LORETA, and LAURA, some incorporating depth weighting [8]. Across various metrics, our approach consistently improves localization accuracy for complex multi-source scenarios while maintaining strong performance for focal configurations. These results underscore the feasibility of deep learning for EEG localization, paving the way for more accurate, data-driven reconstructions of large-scale brain networks, even in the absence of MRI or MEG constraints.

*These authors equally contributed to this work.

C. Buda, B. Gambosi, and L. Astolfi are with the Department of Computer, Control and Management Engineering, Sapienza University of Rome, Italy.

N. Toschi is with the Department of Biomedicine and Prevention, University of Rome Tor Vergata, Italy, with A.A. Martinos Center for Biomedical Imaging, Harvard Medical School, USA, and with the Department of Psychology, School of Biological Sciences, University of Cambridge, UK.

Correspondence to christian.buda@uniroma1.it

II. MATERIALS AND METHODS

A. Forward Modeling and Head Setup

The basis of our simulation environment is a single-subject structural MRI from the publicly available multi-modal dataset in [9]. We processed the anatomical image with FreeSurfer [1] to segment tissues into gray matter, white matter, cerebrospinal fluid, skull, and scalp. Conductivity values were assigned based on standard literature. In order to build the necessary leadfields that map from dipoles in the brain to electrode measurements on the scalp, we generated two distinct forward operators.

The first forward operator *A* was built via DUNEuro [10], which solves the relevant electromagnetic boundary-value problems using finite element approaches. This operator used a 3D mesh representation of the segmented anatomy and placed 51 electrodes with the same layout as patient number 16 in [9]. We uniformly distributed 8196 dipoles (with fixed orientations normal to the cortex) on the white-matter surface. This operator was used exclusively to project synthetic source distributions into simulated scalp EEG.

The second forward operator *B* was constructed with OpenMEEG [11], [12], using a boundary-element based approach and slightly modified conductivity values. Operator *B* was employed in all classical inverse solvers (MNE, sLORETA, eLORETA, LORETA, dSPM, LAURA, etc.). The purpose of using two separate operators is to prevent the the classical methods from having the same exact forward model as the generated data, making the comparison more realistic and minimizing the risk of artificially favoring these approaches.

B. Synthetic EEG Generation

We developed a multi-module pipeline to create synthetic EEG segments that exhibit user-defined spatial and temporal characteristics of the sources. The pipeline is summarized below in paragraphs to highlight the technical approach.

The *spatial module* begins by randomly choosing the number of active regions (from one to three) to reflect the possibility of focal or multifocal generators. For each region, a "center dipole" is selected at random in the following way:

1) A dipole c_1 is selected uniformly at random on the cortex.
2) If needed, a second dipole c_2 is extracted with a probability proportional to the distance to the first center extracted.
3) If needed, a third dipole c_3 is extracted with a probability proportional to the minimum distance to the first two centers extracted.

For each center dipole c_i, a region extent in millimeters is drawn from a uniform distribution (e.g., 20–60 mm), and dditional dipoles p_j^1, p_j^2, p_j^3 within that radial zone are collected into a cloud of contiguous current sources. Each dipole p_j^i is then assigned a spatial coefficient l_j^i, which decreases radially from c_i. This ensures that synthetic generators resemble realistic focal patches rather than single isolated dipoles.

The *temporal module* assigns an autoregressive (AR) time series to every dipole in the head, regardless of whether it is active or not. Each AR process is derived by fitting to plausible source data in order to preserve realistic power spectral features. Each series is then rescaled to a standardized amplitude.

A *synchronization step* modulates the correlation among active dipoles in the same region. Specifically, each dipole's time course is blended with that of its center dipole, weighted by its radial coefficient, i.e. if dipole j is assigned to region i, then

$$p_j(t) \leftarrow l_j^i \cdot c_i(t) + (1 - l_j^i) \cdot p_j(t),$$

where $p_j(t)$ is the time series originally assigned to dipole j. Consequently, a larger l_j^i enhances synchronization with the central dipole. This process establishes a gradient from highly synchronous signals near the center to largely independent signals outside the active regions.

Where two or more active patches overlap, the radial coefficients are normalized so that the overlapping dipole partially synchronizes with both central generators; e.g., if dipole j belongs to both region 1 and 2 then,

$$p_j(t) \leftarrow \frac{l_j^1}{\max\{l_j^1 + l_j^2, 1\}} \cdot c_1(t) + \frac{l_j^2}{\max\{l_j^1 + l_j^2, 1\}} \cdot c_2(t) + (1 - \min\{l_j^1 + l_j^2, 1\}) \cdot p_j(t).$$

This creates a gradient of temporal correlation within each patch, reflecting the spatial continuity often observed in real cortical activations. Dipoles designated as "active" then receive an additional multiplicative boost (e.g., a factor of 10), imposing a controlled ratio between active and background dipoles.

Finally, the *scalp projection* module multiplies the dipole time series by Operator *A*, thereby mapping neural currents onto realistic electrode measurements. The result is a set of synthetic EEG matrices (51 channels $\times$ T time samples), along with a ground-truth map of active dipoles and inactive dipoles (the coefficients l_j^i). By repeating this simulation process with randomized parameters, we assemble a diverse training corpus spanning single and multiple regions, cortical versus subcortical placements, and variable extents.

C. Deep Learning Model Architecture and Training

We formulated the source localization task as predicting a continuous activation coefficient for each of the 8196 dipoles in a given 0.2 s segment of EEG. We used a short time window (0.2 s at 250 Hz, thus 50 time samples $\times$ 51 electrodes) to capture spatiotemporal structure without overly diluting the training with excessive temporal context. The target activation coefficient is can assume any value between 0 and 1, making the learning objective a multi-dimensional regression problem. We adopt a standard L1 loss averaged over the various dipoles.

We chose a convolutional neural network (ConvNet) that processes the 2D EEG array (channel $\times$ time) through multiple 1D convolutional layers, batch normalization, and

ReLU non-linearities. After extracting features, we flatten the final feature maps into a fully connected stage that eventually outputs a 8196-dimensional vector. Each entry in that vector ranges from 0 to 1 via a sigmoid activation. In comparison to purely feedforward network, the convolutional approach effectively exploits local correlations in time. We used a kernel size of 3, with an average pooling to reduce dimensionality. We trained with the Adam optimizer, used moderate weight decay, and employed a learning rate scheduler that reduced the step size on validation plateaus. The training set comprised 5000 synthetic examples, each containing randomly chosen parameters for patch size, patch location, and number of patches. By presenting such a varied dataset to the ConvNet, we aim to endow it with robust generalization to new configurations of cortical generators.

D. Comparison with Classical Inverse Methods

We benchmarked the proposed ConvNet against nine traditional solvers:MNE, dSPM, sLORETA, eLORETA, LORETA, and LAURA (all without orientation or depth weighting) [2]–[5], [13], as well as MNE, dSPM, and sLORETA with orientation constraints and depth weighting (0.2 and 0.8, respectively) [8]. Each method was given the second forward operator (Operator *B*, built with OpenMEEG) and used standard regularization parameters as implemented in MNE-Python [12]. All methods then produced spatiotemporal estimates of dipole currents. We took the norm of each dipole's vector estimate, optionally smoothed in space, normalized the maximum amplitude to 1, and averaged over the 0.2 s time window. This yielded a final 3D distribution of estimated activity for each solver. We thresholded or extracted metrics from these estimates to compare with the known ground-truth distributions.

E. Evaluation Metrics

To evaluate performance comprehensively, we employed metrics that capture different facets of localization accuracy. These included the fraction of the predicted top set that falls within the true region (FractionActive), the peak activity spread (PAS) assessing how concentrated an estimated (single) source is, specialized near-field and far-field AUC scores ($\text{AUC}_{\text{close}}$ and AUC_{far}), and various distance rankings (DR_1, DR_2, DR_3) enumerating how deep in the predicted ranking the true active dipoles appear (giving a measure of how close the method was to correctly identify the first, second, or third center respectively), with DR_{least} indicating how accurately the method identified the least active dipole (adding and indication of whether the other metrics are influenced by an incorrect ranking of the three centers). Baselines included a "Random" predictor that assigns random intensities to dipoles, and a "Perfect" reference given by the exact ground-truth mask. By quantifying performance across multiple metrics and across diverse test scenarios, we can observe both the surface bias of classical methods and the capacity of the ConvNet to localize multiple sources.

III. RESULTS

We tested the trained ConvNet and the classical solvers on a collection of synthetic EEG recordings featuring seven representative configurations (labeled A through G). For better clarity, results corresponding to Regions E to G are presented in the appendix.

These configurations ranged from single large cortical patches, to up to three distinct regions. We generated a 2 minutes EEG recording for each configuration, and then segmented it into 0.2 s windows to run each method on each window, producing ∼650 samples per region. Tables VI, VII, I, II, III, IV, and VIII list quantitative metrics, which are computed as median values across the 650 samples. A subset of visual reconstructions (selected as representatives across the 650 samples) is provided below in Fig. 6,7,2,3,4,5,8. Blue dots represent the true active dipoles, while red patches show the predicted cortical activity.

Additionally, we generated 5000 test sample (each as a 0.2 s recording) to evaluate general performances. Results are shown in table IX.

A comparison between a representative real vs simulated recording is shown in figure 1 for illustrative purposes.

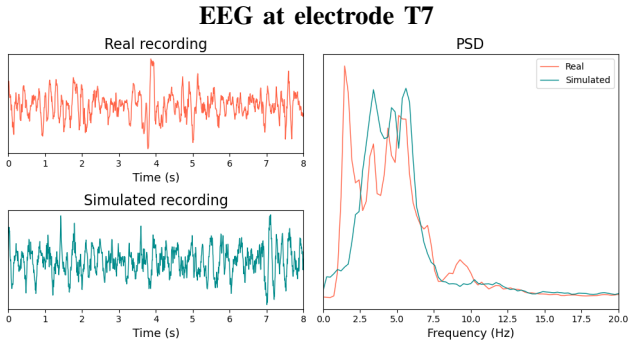

Fig. 1. Comparison of a simulated vs real (resting state) EEG recording at electrode T7. Both time course and PSD are shown.

A. Region A (Double Mixed Size Patches)

Region A displays a medium and a small source of activity far away from each other. Table I summarizes the metrics; Fig. 2 visualizes the reconstructions from the proposed ConvNET and MNE.

Methods	$\text{AUC}_{\text{close}}$	AUC_{far}	FractionActive	DR_{least}	DR_1	DR_2
Random	0.497	0.487	0.029	0.598	0.192	0.598
Perfect	1	1	1	0	0	0
ConvNET	0.881	1.000	0.699	0.041	0.008	0.031
MNE	0.912	0.997	0.751	0.056	0.017	0.051
dSPM	0.610	0.753	0.010	0.402	0.189	0.385
sLORETA	0.796	0.979	0.531	0.131	0.007	0.115
$\text{MNE}_{\text{depthw}}$	0.873	0.999	0.680	0.056	0.010	0.046
$\text{dSPM}_{\text{depthw}}$	0.620	0.755	0.000	0.419	0.192	0.405
$\text{sLORETA}_{\text{depthw}}$	0.799	0.992	0.579	0.173	0.005	0.173
eLORETA	0.815	0.998	0.586	0.104	0.011	0.092
LORETA	0.899	0.988	0.667	0.059	0.025	0.054
LAURA	0.487	0.364	0.000	0.694	0.694	0.331

TABLE I
PERFORMANCE MEASURES ON REGION A.

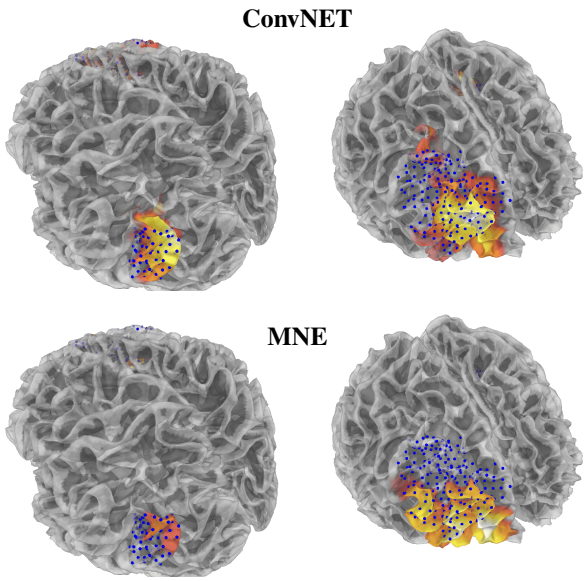

Fig. 2. Reconstruction of Region A using ConvNET (upper figures) and MNE (lower figures). Blue dots indicate the ground truth region, while the colors highlight the highest predicted activation (from highest to lowest: white, yellow, orange, red).

The performances are still high for most methods, indicating that large sources generally don't represent a problem for the standard techniques.

B. Region B (Double Medium Sized Patches)

Region B displays two medium sized sources of activity on opposite sides of the head. Table II summarizes the metrics; Fig. 3 visualizes the reconstructions from the proposed ConvNET and sLORETA.

Methods	AUC_{close}	AUC_{far}	FractionActive	DR_{least}	DR_1	DR_2
Random	0.499	0.562	0.068	0.571	0.571	0.006
Perfect	1	1	1	0	0	0
ConvNET	0.962	1.000	0.916	0.012	0.003	0.008
MNE	0.756	0.991	0.494	0.065	0.029	0.056
dSPM	0.625	0.756	0.141	0.285	0.163	0.249
sLORETA	0.761	0.991	0.474	0.075	0.009	0.044
MNE_{depthw}	0.787	0.995	0.526	0.045	0.008	0.034
$dSPM_{depthw}$	0.618	0.732	0.000	0.306	0.174	0.262
$sLORETA_{depthw}$	0.754	0.999	0.474	0.072	0.007	0.060
eLORETA	0.782	1.000	0.506	0.066	0.007	0.047
LORETA	0.725	0.957	0.430	0.088	0.045	0.082
LAURA	0.698	0.687	0.000	0.339	0.193	0.339

TABLE II

PERFORMANCE MEASURES ON REGION B.

Interestingly, as shown in table II, classical methods struggle to identify correctly both regions, while the network retains good performances.

C. Region C (Triple Medium Sized Patches)

Region C displays three medium sized sources of activity on various sides of the head. Table III summarizes the metrics; Fig. 4 visualizes the reconstructions from the proposed ConvNET and MNE depth-weighted.

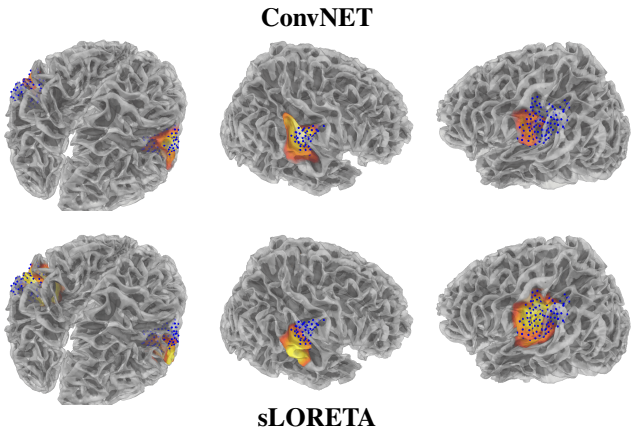

Fig. 3. Reconstruction of Region B using ConvNET (upper figures) and sLORETA (lower figures). Blue dots indicate the ground truth region, while the colors highlight the highest predicted activation (from highest to lowest: white, yellow, orange, red).

Methods	AUC_{close}	AUC_{far}	FractionActive	DR_{least}	DR_1	DR_2	DR_3
Random	0.525	0.500	0.042	0.816	0.296	0.816	0.580
Perfect	1	1	1	0	0	0	0
ConvNET	0.838	0.997	0.640	0.097	0.008	0.059	0.038
MNE	0.779	0.990	0.471	0.104	0.069	0.045	0.046
dSPM	0.549	0.562	0.000	0.509	0.286	0.401	0.361
sLORETA	0.675	0.847	0.347	0.329	0.052	0.069	0.077
MNE_{depthw}	0.764	0.983	0.458	0.106	0.042	0.030	0.028
$dSPM_{depthw}$	0.582	0.544	0.000	0.506	0.313	0.410	0.309
$sLORETA_{depthw}$	0.694	0.945	0.367	0.223	0.071	0.102	0.019
eLORETA	0.691	0.945	0.380	0.214	0.052	0.055	0.057
LORETA	0.769	0.974	0.419	0.132	0.104	0.079	0.059
LAURA	0.538	0.366	0.000	0.793	0.319	0.607	0.792

TABLE III

PERFORMANCE MEASURES ON REGION C.

In this region, the network achieves markedly higher AUC and FractionActive performances, while classical methods struggle to identify correct borders of the regions.

D. Region D (Double Medium Sized Close Patches)

As in Region B, this region displays two medium sized sources of activity; the centers here are chosen to be closer than usual, to evaluate both resolution and to test the network on atypical data. Table IV summarizes the metrics; Fig. 5 visualizes the reconstructions from the proposed ConvNET and MNE depth-weighted.

Methods	AUC_{close}	AUC_{far}	FractionActive	DR_{least}	DR_1	DR_2
Random	0.482	0.537	0.055	0.942	0.541	0.942
Perfect	1	1	1	0	0	0
ConvNET	0.768	0.984	0.505	0.105	0.048	0.037
MNE	0.596	0.742	0.011	0.465	0.307	0.428
dSPM	0.539	0.613	0.000	0.424	0.359	0.360
sLORETA	0.623	0.783	0.143	0.392	0.163	0.278
MNE_{depthw}	0.658	0.698	0.198	0.354	0.071	0.268
$dSPM_{depthw}$	0.552	0.617	0.000	0.341	0.252	0.284
$sLORETA_{depthw}$	0.615	0.696	0.121	0.469	0.166	0.335
eLORETA	0.630	0.756	0.242	0.417	0.157	0.247
LORETA	0.583	0.704	0.000	0.459	0.333	0.435
LAURA	0.305	0.372	0.000	0.727	0.726	0.599

TABLE IV

PERFORMANCE MEASURES ON REGION D.

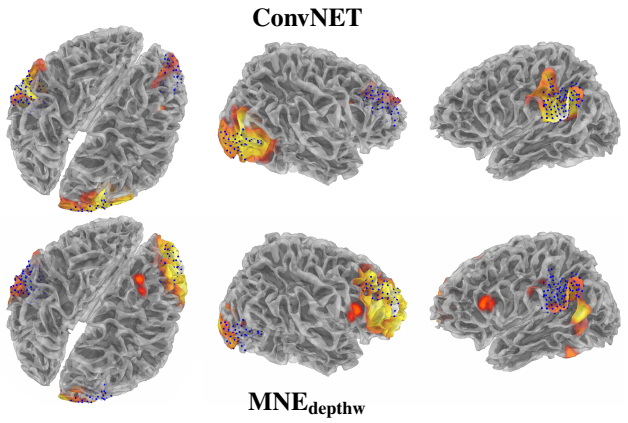

Fig. 4. Reconstruction of Region C using ConvNET (upper figures) and MNE$_{depthw}$ (lower figures). Blue dots indicate the ground truth region, while the colors highlight the highest predicted activation (from highest to lowest: white, yellow, orange, red).

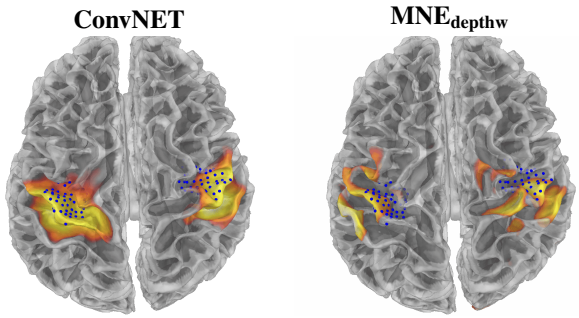

Fig. 5. Reconstruction of Region D using ConvNET (left) and MNE$_{depthw}$ (right). Blue dots indicate the ground truth region, while the colors highlight the highest predicted activation (from highest to lowest: white, yellow, orange, red).

As the distance between the patches approaches the inter-electrode distance the performance degrade noticeably: the network still shows decent reconstruction, but it clearly struggles to identify the two regions correctly (see FractionActive). Meanwhile, all the other methods show high difficulty in identifying the correct sources, with MNE depth-weighted showcasing barely decent performances.

E. Test Set

This test set is composed of 5000 additional 0.2 s recordings with randomly generated activation patterns; these offer a good indication of general performance across all the methods. A more digestible version of the results is shown in table V; the full results can be found in table IX in the appendix.

These results show that, while most methods can offer somewhat decent localization performances, the network generally outperforms classical techniques with decent performances across the board.

IV. DISCUSSION

Overall, results indicate that for large superficial sources, classical inverses perform reasonably well, but the ConvNET typically provides comparable or slightly better spatial specificity. For multiple sources (Regions B to D and G), classical methods often erroneously spread the energy widely, while the ConvNet displays improved accuracy. In particular, metrics such as AUC$_{close}$ and FractionActive reveal that the network consistently places the bulk of its predicted activity in the true regions.

Methods	AUC$_{average}$	FractionActive	DR$_{least}$	DR$_1$	DR$_2$
Random	0.5	0.049	0.691	0.501	0.495
Perfect	1	1	0	0	0
ConvNET	0.973	0.741	0.049	0.011	0.02
MNE	0.847	0.346	0.279	0.105	0.105
sLORETA	0.89	0.454	0.195	0.047	0.085

TABLE V

PERFORMANCE MEASURES ON THE TEST SET. ONLY SELECTED METHODS AND METRICS ARE SHOWN FOR SIMPLICITY. FULL RESULTS CAN BE FOUND IN THE APPENDIX.

These results suggest that deep learning can effectively reduce the single large source bias typical of linear inverse solvers, as evidenced by more accurate localization of multiple sources in scenarios like Region C and Region D. The approach simultaneously retains competitive performance on single regions (see Regions E and F in the appendix), even when the active patches are smaller. One critical advantage of the convolutional network lies in its ability to learn non-linear relationships between scalp potentials and underlying currents, incorporating short-term temporal correlations in the EEG segment (0.2 s in this study).

Classical methods like MNE, sLORETA, and dSPM are time-sample-by-time-sample linear operations (relying on simple averaging over time) and impose constraints that disfavor strong deep generators. Even eLORETA or the use of orientation priors do not entirely resolve the tendency to misplace activity. Our pipeline explicitly trains the network on multiple sources scenarios, thereby teaching it how to interpret subtle multi-channel patterns that arise from different highly active dipoles. The improved fraction of predicted dipoles falling in the correct region and sharper spatial foci underscore that the learned solution can exploit spectral or correlation cues in ways that classical solvers cannot.

At the same time, the simulation environment has limitations. Real EEG data contain various physiological and non-physiological artifacts, such as eye blinks, muscle noise, and environmental interference. Our uncorrelated noise model may not capture these complexities. The geometry and conductivity values of the head model, although based on a real MRI, may deviate further in real practice. Another limitation is that we used only one subject's structural data (with minimal variations in the forward model), so the model does not see large differences in head shape or tissue properties. Extending training to multiple anatomies or employing subject-specific domain adaptation would likely be necessary for broad generalization. Still, the demonstration that a suitably large training set of synthetic data can

produce a robust multi-source solver is highly encouraging; this, combined with the fact that subcortical reconstruction is already possible within deep learning frameworks, paves the way for a subcortical multi-source reconstruction, and maybe even a full electrical activity reconstruction in the entire brain.

V. CONCLUSION

We proposed a deep learning approach to EEG source localization with an emphasis on multiple distinct generators, a notoriously challenging scenario in traditional inverse methods. By using a carefully designed simulation pipeline and training a convolutional neural network on thousands of realistic synthetic examples, we achieved consistently better localization of multiple sources compared to nine classical solvers, while preserving competitive performance for cortical activity. Future work will address subcortical localization, multiple-subject generalization, better modeling of realistic noise and artifacts, and the inclusion of richer physiological constraints in the simulation. These results highlight that end-to-end deep learning can help overcome fundamental biases in EEG source imaging, enhancing the capacity to identify electrical activity noninvasively.

APPENDIX

We leave in the appendix two examples of the performances of the network on single region activations, as well as an example of two distinct regions that are too close to be identified. Moreover, the full performances on the test set are reported.

A. Region E (Single Large Focus)

Region E is a 60 mm extent patch on the left lateral cortex. Table VI summarizes the metrics; Fig. 6 visualizes the reconstructions from the proposed ConvNET and sLORETA.

Methods	AUC_{close}	AUC_{far}	PAS (mm)	FractionActive	DR_{least}
Random	0.500	0.492	66	0.060	0.599
Perfect	1	1	15	1	0
ConvNET	0.930	0.997	18	0.833	0.016
MNE	0.977	1.000	15	1.000	0.006
dSPM	0.693	0.997	23	0.159	0.045
sLORETA	0.944	1.000	21	0.871	0.000
MNE_{depthw}	0.927	1.000	17	0.867	0.022
$dSPM_{depthw}$	0.641	0.991	28	0.043	0.140
$sLORETA_{depthw}$	0.950	1.000	20	0.884	0.001
eLORETA	0.955	1.000	17	0.901	0.002
LORETA	0.971	1.000	15	0.991	0.008
LAURA	0.663	0.615	18	0.000	0.348

TABLE VI
PERFORMANCE MEASURES ON REGION E (LARGE CORTICAL ACTIVATION).

B. Region F (Single Medium Sized Focus)

Region F is a 30 mm extent patch. Table VII summarizes the metrics; Fig. 7 visualizes the reconstructions from the proposed ConvNET and MNE.

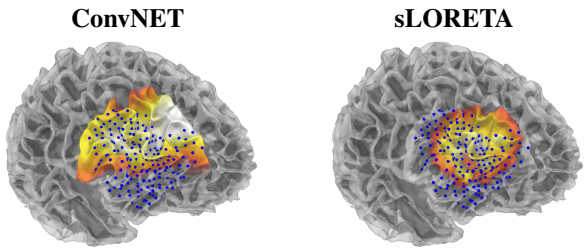

Fig. 6. Reconstruction of Region E using ConvNET (left) and sLORETA (right). Blue dots indicate the ground truth region, while colors highlight the highest predicted activation (from highest to lowest: white, yellow, orange, red).

Methods	AUC_{close}	AUC_{far}	PAS (mm)	FractionActive	DR_{least}
Random	0.481	0.459	66	0.048	0.487
Perfect	1	1	11	1	0
ConvNET	0.974	1.000	12	1.000	0.002
MNE	0.868	1.000	12	0.919	0.012
dSPM	0.493	0.994	19	0.065	0.168
sLORETA	0.917	1.000	25	0.984	0.008
MNE_{depthw}	0.653	1.000	30	0.387	0.084
$dSPM_{depthw}$	0.408	0.975	21	0.000	0.303
$sLORETA_{depthw}$	0.932	1.000	27	0.968	0.010
eLORETA	0.912	1.000	24	0.968	0.014
LORETA	0.832	0.999	14	0.758	0.017
LAURA	0.299	0.575	20	0.000	0.674

TABLE VII
PERFORMANCE MEASURES ON REGION F.

C. Region G (Double Medium Sized Very Close Patches)

As in Region D, this region displays two medium sized sources of activity; the centers here are chosen to be very close with each other, to evaluate the distance at which the sources are indistinguishable from each other. Table VIII summarizes the metrics; Fig. 8 visualizes the reconstructions from the proposed ConvNET and MNE depth-weighted.

D. Test Set

In Table IX the full performances on the test set are shown. Note that metrics D_2 and D_3 are averaged only across those regions that present two or three distinct sources of activations.

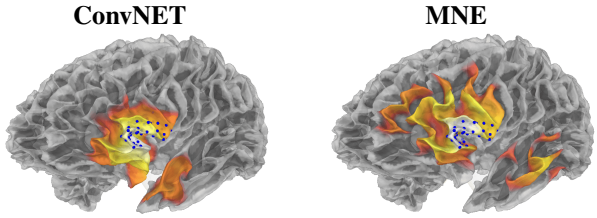

Fig. 7. Reconstruction of Region F using ConvNET (left) and MNE (right). Blue dots indicate the ground truth region, while the colors highlight the highest predicted activation (from highest to lowest: white, yellow, orange, red).

Methods	AUC_{close}	AUC_{far}	FractionActive	DR_{least}	DR_1	DR_2
Random	0.567	0.558	0.054	0.651	0.651	0.360
Perfect	1	1	1	0	0	0
ConvNET	0.918	1.000	0.935	0.030	0.024	0.009
MNE	0.857	0.990	0.739	0.043	0.023	0.041
dSPM	0.628	0.834	0.011	0.273	0.262	0.197
sLORETA	0.809	1.000	0.598	0.043	0.018	0.027
MNE_{depthw}	0.890	0.999	0.815	0.024	0.012	0.019
$dSPM_{depthw}$	0.646	0.863	0.000	0.287	0.272	0.181
$sLORETA_{depthw}$	0.850	1.000	0.739	0.035	0.018	0.021
eLORETA	0.862	1.000	0.783	0.033	0.011	0.027
LORETA	0.820	0.953	0.630	0.078	0.035	0.077
LAURA	0.702	0.744	0.000	0.311	0.302	0.296

TABLE VIII

PERFORMANCE MEASURES ON REGION G.

Methods	AUC_{close}	AUC_{far}	FractionActive	DR_{least}	DR_1	DR_2	DR_3
Random	0.5	0.5	0.049	0.691	0.501	0.495	0.499
Perfect	1	1	1	0	0	0	0
ConvNET	0.973	0.973	0.741	0.049	0.011	0.02	0.031
MNE	0.847	0.846	0.346	0.279	0.105	0.105	0.116
dSPM	0.723	0.723	0.021	0.373	0.252	0.295	0.322
sLORETA	0.89	0.89	0.454	0.195	0.047	0.085	0.120
MNE_{depthw}	0.855	0.857	0.412	0.246	0.076	0.083	0.101
$dSPM_{depthw}$	0.735	0.734	0.0	0.343	0.235	0.275	0.292
$sLORETA_{depthw}$	0.901	0.9	0.48	0.185	0.039	0.069	0.089
eLORETA	0.91	0.91	0.5	0.168	0.036	0.061	0.086
LORETA	0.784	0.784	0.245	0.376	0.179	0.159	0.170
LAURA	0.48	0.479	0.0	0.684	0.502	0.528	0.539

TABLE IX

PERFORMANCE MEASURES ON THE TEST SET.

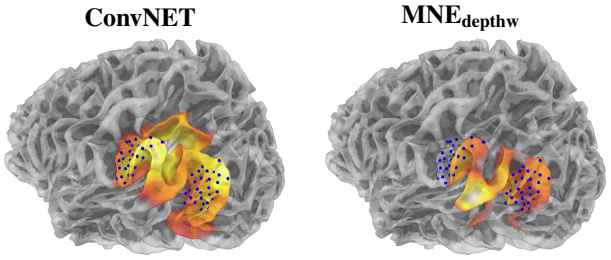

Fig. 8. Reconstruction of Region G using ConvNET (left) and MNE_{depthw} (right). Blue dots indicate the ground truth region, while the colors highlight the highest predicted activation (from highest to lowest: white, yellow, orange, red).

ACKNOWLEDGMENT

We thank the open-access data providers and the developers of FreeSurfer, DUNEuro, and OpenMEEG.

REFERENCES

[1] Dale, A., Fischl, B. & Sereno, M. Cortical surface-based analysis. I. Segmentation and surface reconstruction. *NeuroImage*. **9** pp. 179-194 (1999)

[2] Hämäläinen, M. & Ilmoniemi, R. Interpreting magnetic fields of the brain: minimum-norm estimates. *Med. Biol. Eng. Comput.*. **32** pp. 35-42 (1994)

[3] Pascual-Marqui, R. Standardized low resolution brain electromagnetic tomography (sLORETA): Technical details. *Methods Find Exp Clin Pharmacol.*. **24**, 5-12 (2002)

[4] De Peralta-Menendez, R. & Gonzalez-Andino, S. A critical analysis of linear inverse solutions to the neuroelectromagnetic inverse problem. *IEEE Trans. Biomed. Eng.*. **45**, 440-448 (1998)

[5] Dale, A., Liu, A., Fischl, B., Buckner, R., Halgren, E. & Others Dynamic Statistical Parametric Mapping: Combining fMRI and MEG for High-Resolution Imaging of Cortical Activity. *Neuron*. **26**, 55-67 (2000)

[6] Sun, R., Sohrabpour, A., Worrell, G. & He, B. Deep neural networks constrained by neural mass models improve electrophysiological source imaging of spatiotemporal brain dynamics. *Proc. Natl. Acad. Sci. U.S.A.*. (2021)

[7] Hecker, L., Rupprecht, R., Tebartz Van Elst, L. & Kornmeier, J. Convdip: a convolutional neural network for better EEG source imaging. *Front. Neurosci.*. **15** pp. 569918 (2021)

[8] Lin, F., Belliveau, J., Dale, A. & Hämäläinen, M. Distributed Current Estimates Using Cortical Orientation Constraints. *Hum. Brain Mapp.*. **27** pp. 1-13 (2006)

[9] Telesford, Q., Gonzalez-Moreira, E., Xu, T. & Others An open-access dataset of naturalistic viewing using simultaneous EEG-fMRI. *Sci Data*. **10** pp. 554 (2023)

[10] Schrader, S., Westhoff, A., Piastra, M., Miinalainen, C., Engwer, C. & Others DUNEuro – A software toolbox for forward modeling in bioelectromagnetism. *PLoS ONE*. **16**, e0252431 (2021)

[11] Gramfort, A., Papadopoulo, T., Olivi, E. & Clerc, M. OpenMEEG: Open-source software for quasistatic bioelectromagnetics. *BioMed Eng OnLine*. **9** pp. 45 (2010)

[12] Gramfort, A., Luessi, M., Larson, E., Engemann, D., Hämäläinen, M. & Others MEG and EEG data analysis with MNE-Python. *Front. Neurosci.*. **7**, 1-13 (2013)

[13] Pascual-Marqui, R. Discrete, 3D distributed, linear imaging methods of electric neuronal activity. Part 1: Exact, zero error localization. *Math. Physics Biol. Physics Neurons Cogn.*.